catalysts

MDPI

Article

Insight into the Piezo-Photocatalytic Degradation Mechanism of Organic Contaminant by Chromium-Doped Bismuth Ferrite Thin Film

Roxana Jijie [1], Marius Dobromir [1], Teodora Matei [2], Ioana-Laura Velicu [2], Valentin Crăciun [3,4], Georgiana Bulai [5,*] and Vasile Tiron [1,*]

[1] Research Center on Advanced Materials and Technologies, Department of Exact and Natural Science, Institute of Interdisciplinary Research, Alexandru Ioan Cuza University of Iasi, 700506 Iasi, Romania; roxana.jijie@uaic.ro (R.J.); marius.dobromir@uaic.ro (M.D.)
[2] Faculty of Physics, Alexandru Ioan Cuza University of Iasi, 700506 Iasi, Romania; dorateom@yahoo.com (T.M.); laura.velicu@uaic.ro (I.-L.V.)
[3] National Institute for Laser, Plasma and Radiation Physics, 077125 Măgurele, Romania; valentincr5@gmail.com
[4] Extreme Light Infrastructure for Nuclear Physics, 077125 Măgurele, Romania
[5] Integrated Center of Environmental Science Studies in the North-Eastern Development Region (CERNESIM), Department of Exact and Natural Science, Institute of Interdisciplinary Research, Alexandru Ioan Cuza University of Iasi, 700506 Iasi, Romania
* Correspondence: georgiana.bulai@uaic.ro (G.B.); vasile.tiron@uaic.ro (V.T.)

Abstract

Piezo-enhanced photocatalysis is progressively considered an eco-friendly technology for contaminant removal, harvesting not only solar energy but also mechanical vibrations found in nature. Multiferroic materials present a coupled effect of various properties and can potentially increase the applicability of this process. In this study, Cr- doped bismuth ferrite thin film was deposited on $SrTiO_3$ substrate by HiPIMS, and its photo-, piezo-, and piezo-photocatalytic efficiencies in Rhodamine B (RhB) degradation were analyzed. The highest removal percentage was found under the simultaneous exposure of visible light and mechanical vibrations, reaching 86.2% after 180 min. The calculated efficiencies for photo- and piezocatalysis were 12.2% and 83.7%, respectively. The rate constant (k) for piezo-photocatalysis was 16.1 times higher than that found during photocatalytic experiments. To assess the contribution of each reactive species to the decomposition process, different reagents were added to the Rhodamine B contaminated solution. The results revealed that when p-benzoquinone was used, the degradation efficiency declined significantly from 86.2% to 37.6%, suggesting that superoxide radicals ($O_2^{\bullet -}$) play a key role in decomposing RhB molecules. The structural, chemical, optical, and ferroelectric changes caused by the catalytic processes were analyzed and linked to the proposed degradation mechanisms. The poor photocatalytic efficiency was linked to an improper band structure and an improper polarization orientation of the ferroelectric domains in the as-deposited film. The degradation mechanisms in piezo-photocatalysis were driven partly by the band bending caused by mechanical vibrations and partly by the reorientation of the induced polarization of the domains in the unstrained film.

Keywords: bismuth ferrite; HiPIMS; piezo-photocatalysis; scavenger tests; degradation mechanism; piezoelectric/ferroelectric properties

Check for updates

Academic Editor: Xiufang Chen

Received: 30 March 2026
Revised: 20 April 2026
Accepted: 23 April 2026
Published: 25 April 2026

Copyright: © 2026 by the authors. Licensee MDPI, Basel, Switzerland. This article is an open access article distributed under the terms and conditions of the Creative Commons Attribution (CC BY) license.

1. Introduction

In recent years, there has been significant interest in advanced oxidation processes occurring during photocatalytic and piezocatalytic experiments, as these methods are considered promising for pollutant removal. Once charge carriers are generated, achieving efficient mobility and reducing recombination processes are crucial for creating more active sites on the catalyst's surface, which facilitate the decomposition process. The focus on heterojunction-based systems is driven by their high efficiency in degrading organic pollutants [1]. In this context, the built-in electric field separates the photo-generated carriers and directs their migration within a thin layer at the interface between the two semiconductors, leaving the electrons and holes generated in the bulk of the material largely unaffected. This limitation can be addressed by using ferroelectric materials. The polarization-induced electric field in ferroelectrics can, in some cases, be up to two orders of magnitude stronger than the separation field in a typical p-n junction and, most importantly, extends across the entire material [2]. Bismuth ferrite is the only multiferroic material at room temperature and has a high Curie point, large spontaneous polarization (>100 $\mu C/cm^2$) and a piezoelectric coefficient and a suitable optical band gap for solar energy conversion application [3]. However, depending on the synthesis method, its photocatalytic performance can be constrained by the high recombination rate of the electrons (e^-) and holes (h^+) generated during light irradiation. This issue can arise from the presence of intrinsic point defects, impurities, surface defects, dislocations, and grain boundaries within the material [4–7]. Bismuth ferrite has a wide range of possible crystallographic lattices. Depending on the type of internal stress present in the material, its structure can vary from rhombohedral (un-strained sample) to orthorhombic (tensile strain) or tetragonal (compressive strain) [8]. Thus, when thin films are studied, the substrate type can have a significant effect on the properties of the grown sample. Our previous study revealed that the bismuth ferrite-based thin films obtained in the same conditions presented various crystallographic structures when deposited on different substrates [9]. Besides improving the multiferroic and magnetic properties, ion doping can also enhance solar power conversion efficiency and photocatalytic efficiency. For photovoltaic application, one of the highest solar power conversion efficiencies (8.1%) was reported for chromium-doped bismuth ferrite thin films [10]. Cation substitution can tailor the band gap of the $BiFeO_3$ and promote the separation of photo-generated charge carriers by reducing part of the recombination sites. The enhancement of power conversion efficiency by cation substitution is due to a narrower band gap and reduced leakage current. The leakage current is related to the presence of excessive oxygen vacancies. For photocatalytic application, a narrower band gap enhances the light absorption capability and the formation of more electron–hole pairs available for the catalytic degradation process, while the substitution of iron by chromium hinders the electron–hole recombination processes due to reduced oxygen vacancies. The degradation performance of a material is significantly influenced not only by the width of the band gap but also by its position relative to the oxidation and reduction potentials [11]. Thus, even though enough charge carriers reach the valence (VB) and conduction bands (CB), they cannot participate in the water decomposition processes if the corresponding band energy levels are not appropriately positioned. The photo-generated electrons in a less negative CB than the standard reduction potential of $O_2/O_2^{\bullet -}$ cannot reduce the O_2 in $O_2^{\bullet -}$. Similarly, the photo-generated holes in a less positive VB than the $HO^{\bullet}/HO^-$ potential cannot oxidize the HO^- to $HO^{\bullet}$. As a result, the photocatalytic performance of the studied material is greatly diminished.

In piezocatalysis, however, the application of mechanical vibrations overlays an induced polarization field onto the intrinsic field, providing an additional driving force for the efficient separation and transport of generated charge carriers throughout the catalyst. Furthermore,

this field can even alter the band structure of the material, making it more energetically favorable for the formation of hydroxyl and superoxide radicals. As a result, the degradation efficiency of the studied materials can be significantly improved when subjected simultaneously to both light and mechanical vibrations. Under these conditions, both solar energy and low-frequency mechanical energy sources found in nature, such as wind, water waves, sonic waves, and atmospheric pressure, can be harnessed. The processes involved are complex, requiring detailed and systematic studies to identify the specific chemical reactions that lead to pollutant decomposition. In this context, our study focuses on the degradation of RhB using a chromium-doped bismuth ferrite (BFCO) thin film, under three different conditions: visible light alone, ultrasonic vibration alone, and their combined effect. STO was chosen as the substrate because it can act as a seeding layer to provide a perovskite structure template for the growing film, enhancing the textured growth of BFCO thin film. Although thin film-based catalysis has, in some cases, fewer active sites than the micro/nanoparticles-based ones (and thus, sometimes, presents poor degradation efficiency), these can also be more easily recovered and reused. In addition, using proper deposition technique, very large surfaces can be coated with a catalytic thin film. A possible piezo-photocatalytic degradation mechanism was proposed based on XRD, XPS and PFM observations before and after the piezo-photocatalysis tests, combined with the results of the trapping experiment, where different scavengers are added during piezo-photocatalysis tests.

2. Results and Discussions

2.1. Piezo-Photocatalytic Properties

The photo-, piezo-, and piezo-photocatalytic activities of the BFCO/STO sample were investigated by assessing the degradation of RhB dye under light irradiation and/or mechanical vibrations, as shown in Figure 1a–c. The initial step involved analyzing the stability of the organic contaminant in the prepared solution under the same exposure conditions but without the catalyst. Approximately 9.2% of RhB dye was removed within 180 min, using simultaneous visible light and ultrasonic vibrations, in the absence of the catalyst. Numerous studies in the literature have investigated the photocatalytic properties of BFO-based materials. For instance, Boughelout et al. assessed the photocatalytic activity of $Bi_{0.98}Ba_{0.002}FeO_3$ thin film, synthesized by a combined sol–gel and spin-coating approach, under natural sunlight, achieving 81% degradation of RhB [12]. Similarly, BFO films deposited on stainless steel mesh surfaces are effective catalysts for the degradation of organics dye, completely degrading RhB within 150 min [13]. Ramezanalizadeh and Manteghi demonstrated that BFO/$CuWO_4$ particles are promising for achieving high photocatalytic efficiency under visible light conditions [14]. In a previous study, the screen-printed p-n BiOCl/$BiFeO_3$ composite exhibited remarkable RhB degradation of 92% after 150 min under visible light [15]. In this work, when the catalyst was exposed to visible light, the RhB degradation efficiency reached only 12% after 180 min, indicating limited photocatalytic activity. This low degradation performance indicates that visible light alone is insufficient to generate charge carriers that effectively participate in the oxidative and reduction reactions required for dye decomposition. Lan et al. ascribed this behavior to an unsuitable band structure or rapid recombination rate of charge carriers [8]. Similar results were reported by Jing et al. [3]. Subsequently, the degradation efficiency of the film was evaluated under simultaneous light irradiation and mechanical vibrations. Considering the piezoelectric nature of STO, the piezo-photocatalytic activity of the substrate alone was first tested, revealing a 34.55% efficiency in dye removal after 180 min. In contrast, the BFCO/STO showed a significantly enhanced degradation efficiency of 83.7% under mechanical vibrations, which is 2.4 times higher than that of the bare substrate and 6.9 times higher than its photocatalytic performance. This improvement can be attributed to the piezoelectric potential generated by the mechanical waves, which

acts as a polarization field, efficiently separating the charge carriers and enhancing the degradation reactions at the catalyst surface. Additionally, the piezoelectric polarization field can elevate the conduction band (CB), allowing more piezo-electrons to participate in reduction reactions [16]. The degradation efficiency further increased to 86.2% when both visible light and mechanical vibrations were applied. The $-\ln(C/C_0)$ vs. time plots show a linear relationship, indicating that the photo-, piezo-, and piezo-photodegradation of RhB by the studied catalyst follows a pseudo-first-order kinetic model. The photodegradation rate constant was estimated at 0.7×10^{-3} min^{-1}, while the rate constant for piezocatalytic experiments was two orders of magnitude higher, reaching 10.1×10^{-3} min^{-1}. The highest rate constant (11.3×10^{-3} min^{-1}) was achieved under simultaneous visible light and mechanical vibrations, which is 16.1 times greater than that from photocatalysis alone. These results are consistent with previous studies on various BFO-based catalysts [3,11], which report a higher rate constant for piezo-photocatalysis compared to individual photo- or piezocatalysis. Moreover, Figure 1d demonstrates the stability and reusability of the catalyst, showing even better degradation performance for the next three consecutive cycles. The results revealed that during the catalysis tests, the contribution of RhB dye adsorption onto the surface of the sample or reactor is negligible, with a 2–3% decrease in absorbance at 554 nm after 30 min in the dark. However, to evaluate the degree of RhB dye adsorption onto the film surface, the BFCO/STO catalyst was characterized by FTIR spectroscopy before and after catalytic reactions. The experimental results show no change in the FTIR spectra (Figure S1), indicating that the adsorption of RhB dye onto the catalyst surface is unnoticeable. Moreover, FTIR analysis confirms the structural stability of the BFCO/STO after the catalytic reactions.

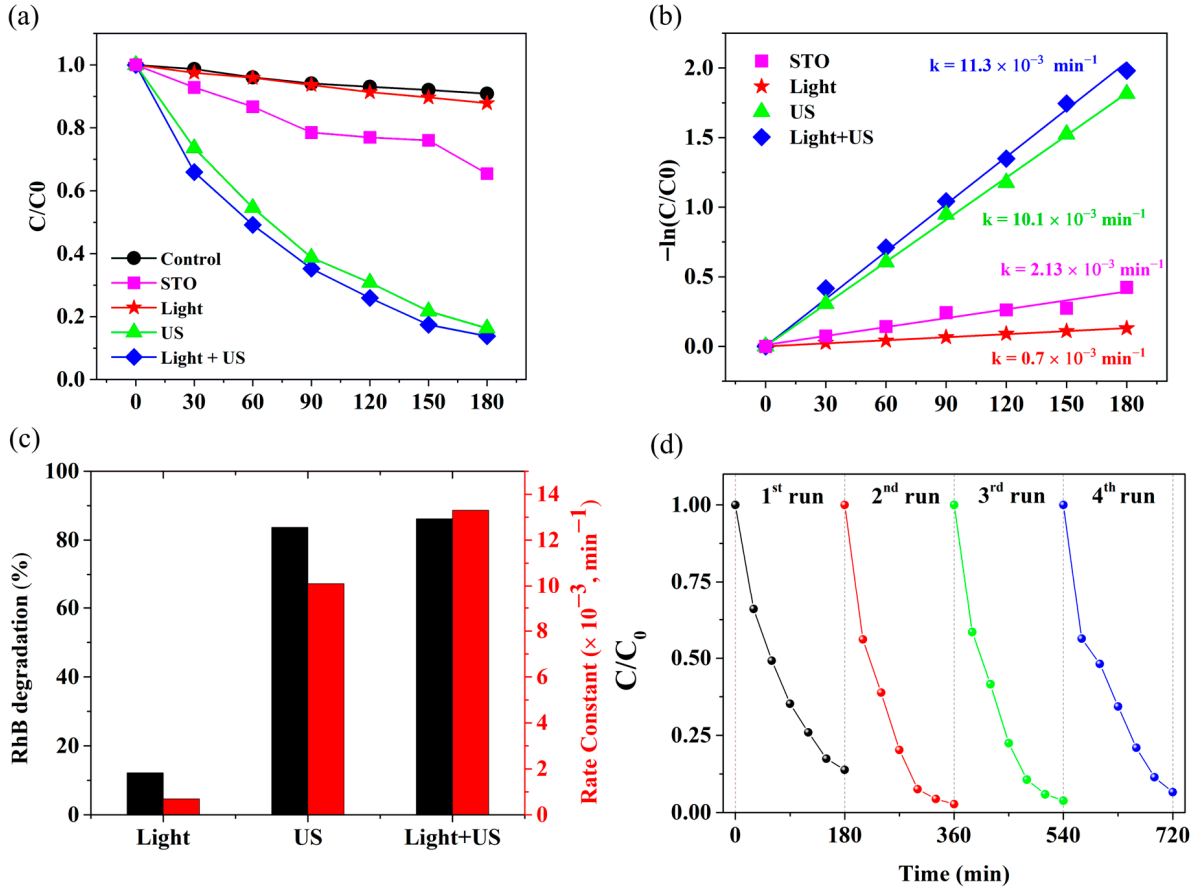


Figure 1. Catalytic efficiency and reusability of the sample under ultrasonic vibrations and light irradiation alone and simultaneously: (**a**) the time-dependent RhB removal curves, (**b**) the first-order kinetic fitting plots, (**c**) the RhB degradation performance and kinetic rate constant (k) after 180 min exposure time and (**d**) the piezo-photocatalytic process stability for four runs.

2.2. Piezo-Photocatalytic Degradation Mechanism

2.2.1. Investigation of the Main Reactive Species Involved in the Piezo/Photocatalytic Degradation of RhB Dye

Based on the degradation results presented above, subsequent trapping tests were performed to investigate the involvement of various active species in the piezo-photocatalytic degradation of RhB dye. Quenching experiments were conducted using BQ, IPA, NaN_3 and EDTA-2Na to suppress the contribution of $O_2^{\bullet-}$, $HO^{\bullet}$, $^1O_2$ and h^+, respectively [3,11,17–22]. Figure 2a–d illustrate the effect of these quenching agents on the dye degradation efficiency. As shown in the time-dependent removal curves (Figure 2a), the piezo-photocatalytic efficiency was significantly reduced when BQ and NaN_3 were added into the solution, while only a slight variation was observed in the presence of EDTA-2Na. The addition of BQ decreased the RhB removal efficiency over the BFCO/FTO sample from 86.2% to 37.6% (↓48.6%), indicating that $O_2^{\bullet-}$ are the primary active species involved in the degradation process. This finding is consistent with previous reports on the degradation of sulfamethoxazole over $Bi_2Fe_4O_9$ nanosheets [23], RhB over bismuth ferrite-based composites [24], and flexible $MoSe_2$/PVDF composite foam [25]. When NaN_3 and IPA were introduced into the solution, the degradation efficiency dropped to 48.9% (↓37.3%) and 65.8% (↓20.4%), suggesting that singlet oxygen ($^1O_2$) and hydroxyl radicals ($HO^{\bullet}$) also contribute to the decomposition of RhB dye. In contrast, the results indicate that h^+ does not directly contribute to dye degradation, in agreement with previous findings reported by Lan et al. for La-doped bismuth ferrite multiferroics [11]. Similarly, the piezo-photodegradation rate constant decreased from 11.3×10^{-3} min^{-1} to 9.31×10^{-3}, 5.81×10^{-3}, 4.28×10^{-3}, and 2.4×10^{-3} with the addition of EDTA-2Na, IPA, NaN_3 and BQ to the RhB solution, respectively. These results suggest that RhB degradation via piezo-photocatalysis is primarily driven by reactive oxygen species (ROS) and follows the order $HO^{\bullet} < {}^1O_2 < O_2^{\bullet-}$. Our findings are in line with previous studies, which also suggest that ROS are the dominant active species involved in the piezo-photocatalytic degradation of organic contaminants. For instance, Hu et al. demonstrated that $HO^{\bullet}$, $^1O_2$ and $O_2^{\bullet-}$ contribute to the piezo-photocatalytic removal of carbamazepine (CBZ) by Au-decorated bismuth oxybromide [26]. Similarly, a combined influence of $HO^{\bullet}$ and $O_2^{\bullet-}$ was observed during the degradation of CBZ and RhB using La-doped BFO-based multiferroics [11], BVO/BFO [3] and $Na_{0.5}Bi_{0.5}TiO_3$ micro-crystals.

2.2.2. XRD Analysis Before and After Piezo-Photocatalysis

The structural characteristics of the deposited thin film, both before and after piezo-photocatalysis tests, were studied using XRD. The obtained diffractograms are shown in Figure 3. Two sets of peaks were observed in both cases: one corresponding to the hexagonal structure of $BiFeO_3$ with R3c space group (ICSD card no. 98-015-7424), and the other one associated with the monoclinic phase of the same material with C1m1 space group (ICSD card no. 98-016-8320). No residual or secondary phases were detected in the investigated samples. The perovskite structure was also confirmed by Rutherford Backscattering pectrometry (RBS) measurements. The stoichiometry of the BFCO thin film determined by RBS (with a 4–5% accuracy) was $Bi_{0.19}Fe_{0.14}Cr_{0.5}O_{0.62}$, indicating a Bi/(Fe+Cr) ratio of 1:1 and a perovskite-type structure. The substitution of iron by chromium may enhance the photo-piezocatalysis process due to reduced oxygen vacancies. Oxygen vacancies with optimal concentration introduce new energy levels (as donor defects) within the bandgap, which act as trapping sites that suppress electron–hole recombination and enhance photo-piezocatalysis. In bulk form, bismuth ferrite has a distorted rhombohedral type structure with a ferroelectric polarization along the [111] pseudocubic direction. The unit cell can also be viewed as a hexagonal prism with the c axis [001] parallel to the diagonal of the

pseudocube [111] [27,28]. However, in thin film form, the strain induced by the substrate type, energetic ion bombardment or temperature can determine the formation of a structure with a reduced symmetry [8,29]. Theoretical and experimental studies revealed that monoclinic structures are energetically favorable in such cases [8,30,31]. Furthermore, according to the study of Chen et al. [32], the monoclinic type symmetry of $BiFeO_3$ arises from in-plane biaxial strain and may serve as a structural bridge linking different crystallographic structures of the same material [33]. Additionally, in the as-deposited sample, the diffraction lines of the hexagonal phase indicated the formation of a polycrystalline film. However, those of the monoclinic structure exhibited preferential crystallographic growth directions along the (111) planes. The crystallites sizes of the two phases were found to be similar. These sizes were estimated using the Sherrer equation, considering the main diffraction lines of each structure. Mean values of 19 nm and 15 nm were found for the monoclinic and hexagonal phases, respectively. After the piezo-photocatalytic degradation experiments, the contribution of the monoclinic phase to the overall diffraction signal was significantly reduced (see the inset of Figure 3). Additionally, both (111) and (222) peaks shifted to higher 2θ angles, indicating a lattice strain relaxation. The crystallite size of the hexagonal structure remained around 16 nm. The changes revealed by XRD are likely caused by the mechanical vibrations applied during the piezo-photocatalytic degradation of RhB. The study of Zeches et al. showed that bismuth ferrite has the ability to morph into allotropic variations, and the stability of these forms is governed by the imposed strain [34]. Both electric field and strain can induce phase transformations and consequently affect the piezoelectric properties of the material [35–37]. The applied ultrasonic waves may have triggered a reorganization of the unit cells into a less strained configuration, thus causing an irreversible phase transition process from a monoclinic to a hexagonal structure.

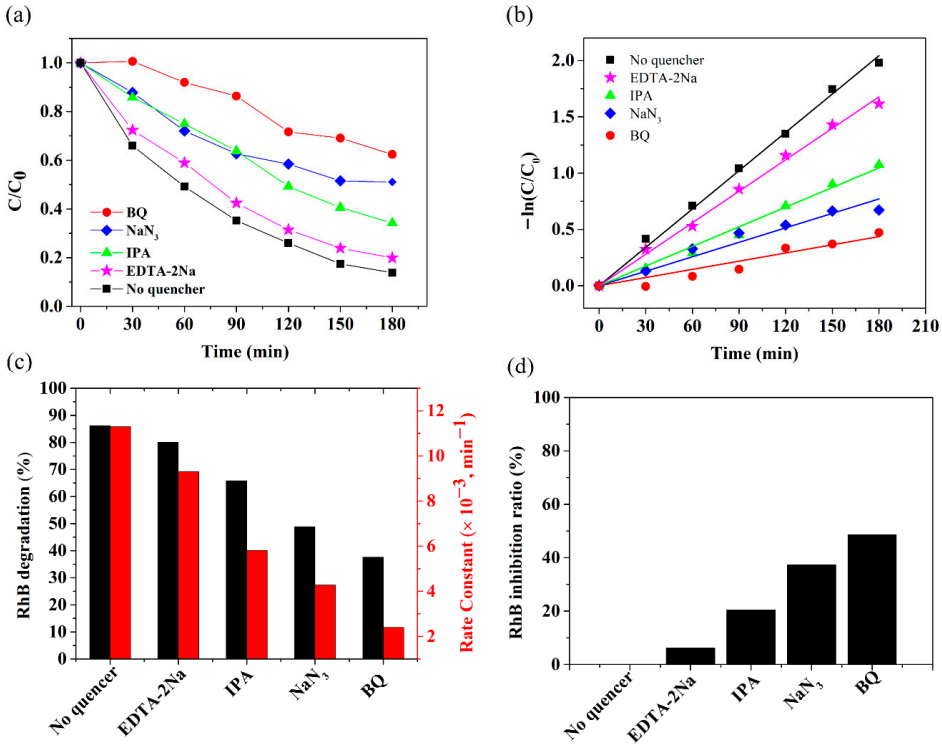


Figure 2. Quenching experiments on the RhB degradation under simultaneous visible light irradiation and ultrasonic vibration (BQ for $O_2^{\bullet -}$, NaN_3 for $^1O_2$, IPA for •OH and EDTA-2Na for h^+): (**a**) the RhB degradation curves, (**b**) the corresponding first-order kinetic fitting plots, (**c**) the RhB degradation efficiency and kinetic rate constant (*k*) after 180 min exposure time and (**d**) the inhibition ratio of RhB degradation in the presence of different quenchers.

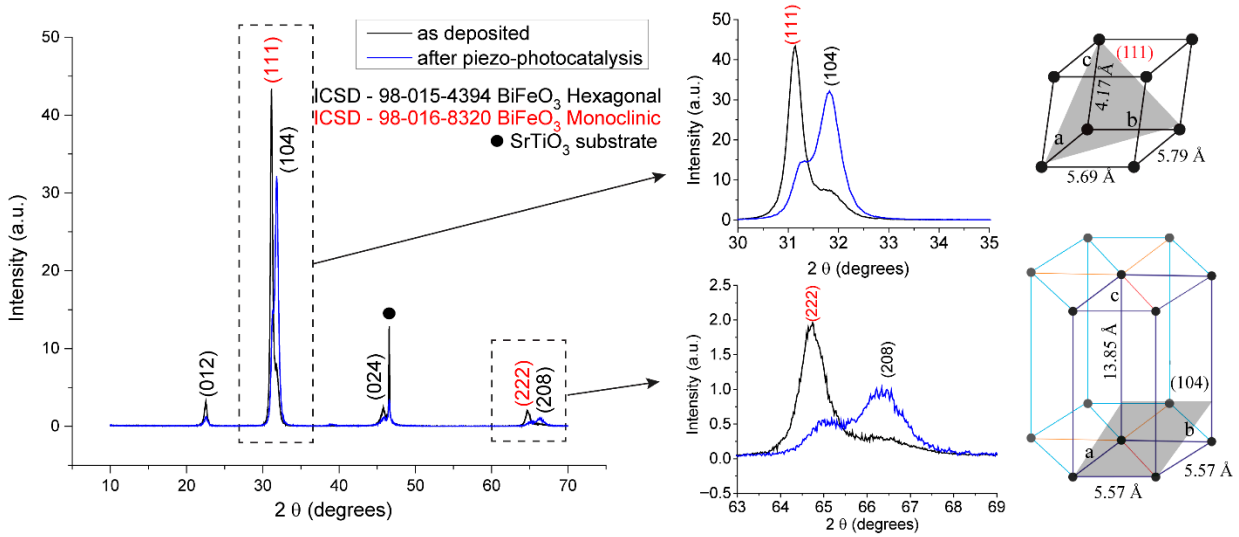


Figure 3. XRD results of the BFCO thin film before and after piezo-photocatalysis experiments.

2.2.3. XPS Analysis Before and After Piezo-Photocatalysis

To better understand the active sites involved in the decomposition process, XPS measurements were conducted before and after the piezo-photocatalysis. The presence of Bi, Fe, Cr, and O on the sample surface was confirmed in both cases, as shown in Figure 4. The spectra were deconvoluted to evaluate the contribution of each ionic state to the overall results. For the as-deposited sample, the slight asymmetry in the Bi 4f7/2 and 4f5/2 peaks (Figure 4a) indicates the presence of two ionic states: Bi^{3+} (at 158.71 eV and 163.97 eV) and Bi^{5+} (at 159.69 eV and 165.04 eV). These states were also detected after piezo-photocatalysis experiments. The presence of both ion types was previously reported by Su et al. in bismuth ferrite ($Bi_2Fe_4O_9$) nanosheets obtained via a hydrothermal method [15,19]. The Bi^{3+}/Bi^{5+} ratio decreased from 14.95 to 7.22 following the piezo-photodegradation, indicating that some Bi^{3+} on the sample surface was oxidized to Bi^{5+} during the dye degradation process.

The deconvolution of Fe2p 3/2 and 1/2 confirmed the presence of both Fe^{2+} and Fe^{3+} ions on the surface of the as-deposited sample (Figure 4b) [38,39]. In the XPS high-resolution spectrum of Fe-2p recorded after catalysis tests (Figure 4b'), besides characteristic Fe^{2+} and Fe^{3+} peaks, two associated satellite peaks appear at 718.8 eV and 731.6 eV. These satellite peaks are associated with Fe^{2+} $2p_{3/2}$ and Fe^{2+} $2p_{1/2}$ main peaks, respectively [40]. The percentage of Fe^{2+} decreased from 67.9% to 57.0% after piezo-photocatalysis, indicating an oxidation process and the active involvement of Fe^{2+}-Fe^{3+} electronic transfer in water decomposition. For Cr2p 3/2 and 1/2, XPS results revealed the presence of Cr^{3+} (at 575.88 eV and 585.26 eV) and Cr^{6+} (at 578.90 eV and 587.76 eV) ions on the sample surface before the dye degradation experiments (Figure 4c). Similar ion types were also observed by Wu et al. in double-perovskite Bi_2FeCrO_6 ceramics [41]. The peaks associated with Cr^{6+} become much more pronounced, and their presence in the overall spectra is more noticeable after piezo-photocatalysis. This suggests that additional oxidation reactions are occurring on the catalyst surface during the experiment. In addition, two satellite peaks appear (at 580.1 eV and 589.6 eV) in the XPS high-resolution spectrum of Cr-2p recorded after catalysis tests (Figure 4c'), which are associated with Cr^{3+} $2p_{3/2}$ and Cr^{3+} $2p_{1/2}$ main peaks.

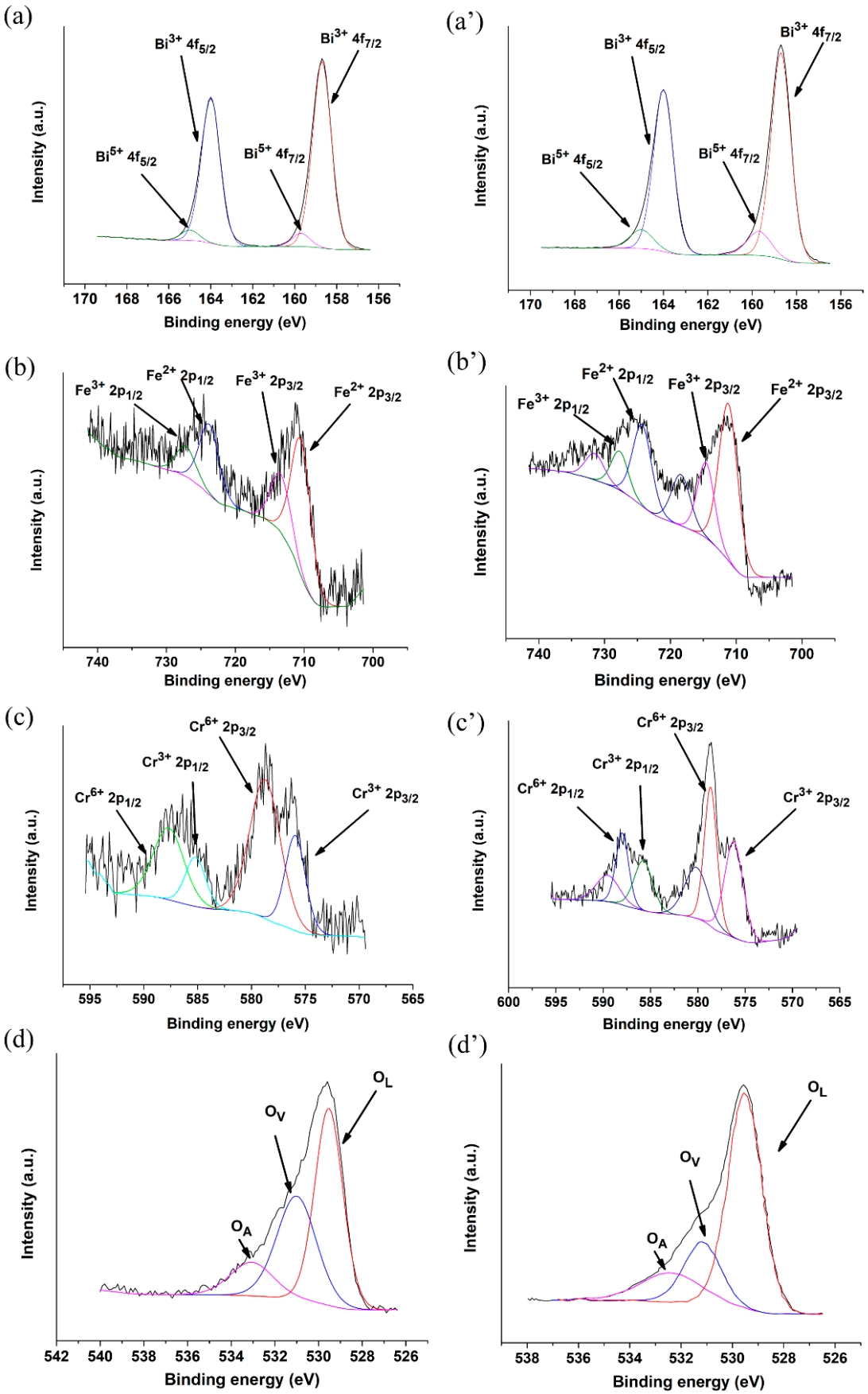


Figure 4. XPS deconvoluted spectra of the BFCO thin film before (left side—(**a**–**d**)) and after (right side—(**a′**–**d′**)) piezo-photocatalysis experiments.

The O1s spectrum (Figure 4d) of the fresh thin film was deconvoluted into three peaks at 529.55 eV, 531.04 eV, and 533.04 eV assigned to lattice oxygen (O_L), surface oxygen vacancies (O_V), and adsorbed oxygen (O_A), respectively [1,3,11,23]. Wu et al. deconvoluted the asymmetric O1s peak observed for Bi_2FeCrO_6 ceramics into three peaks, located at 528.8, 530.6, and 533.0 eV [41]. The first two peaks were attributed to O^{2-} ions in the lattice sites of [FeO_6] and [CrO_6] octahedrons, while the third peak was linked to oxygen in a deficient state, indicating the instability of O^- bound to Bi, Fe, and Cr in the Bi_2FeCrO_6 ceramics. While the percentages of the O_L assigned peaks showed only slight changes after the piezo-photocatalytic process, the percentages of O_V decreased from 36.8% to 24.4%. The reduced oxygen vacancies act as trapping sites that suppress electron–hole recombination and enhance photo-piezocatalysis. Meanwhile, surface absorbed oxygen increased from 13.1% to 21.45%. The study of Zhao et al. revealed that the photocatalytic performance of different ABO_3 perovskite oxides is proportional to the surface absorbed oxygen [42].

2.2.4. Piezoelectricity and Ferroelectric Responses Before and After Piezo-Photocatalysis

Piezoresponse force microscopy (PFM) was used to examine the ferroelectric and piezoelectric properties of the BFO thin film catalyst both before and after piezo-photocatalysis tests. Figure 5a–c displays the two-dimensional (2D) topography, out-of-plane piezoresponse amplitude, and phase images of the sample before the dye degradation experiments. The topography does not match the PFM amplitude and phase images, suggesting that the features seen in the latter images are due to the piezoelectric properties of the sample. The uniform contrast in the PFM amplitude and phase images indicates that the piezoelectric domains have a consistent response and polarization/orientation. Local PFM polarization switching spectroscopy was used to assess ferroelectricity and piezoelectricity at two distinct points (marked as A and B in Figure 5c). The piezoelectric amplitude curves at both points exhibit similar butterfly-shaped loops with a maximum amplitude of approximately 430 pm under a ±10 V DC bias voltage (Figure 5d,e). Additionally, a well-defined 160° phase angle inversion and wide hysteresis loop are observed, demonstrating the presence of ferroelectric switching and consistent orientation of ferroelectric domains at both points.

The width of the phase hysteresis loops and the gap between PFM amplitude curves are approximately 5 V. The piezoresponse curve shows that the maximum effective piezoelectric coefficient (d_{33}) is 100 pm/V, measured at the applied voltage of 5 V.

Figure 5a′–c′ shows the topographic, out-of-plane piezoresponse amplitude, and phase images of the BFCO sample after piezo-photocatalysis tests. In this case there was a noticeable change in the topographic image, showing improved grain refinement (Figure 5a′). Additionally, the PFM amplitude image reveals distinct piezoelectric domains and responses on a local scale (Figure 5b′). The phase angle between the applied tip bias and the piezoresponse signal highlights different polarizations and orientations of the piezoelectric domains in the BFCO thin film (Figure 5c′). These results suggest that mechanical vibrations lead to a lattice strain relaxation process, causing some piezoelectric domains to reverse. XRD measurements also support this statement, showing changes in crystallographic properties during the degradation tests: shifting from a dominant structure with a (111) plane orientation to a polycrystalline phase with the highest intensity ascribed to the (104) diffraction line.

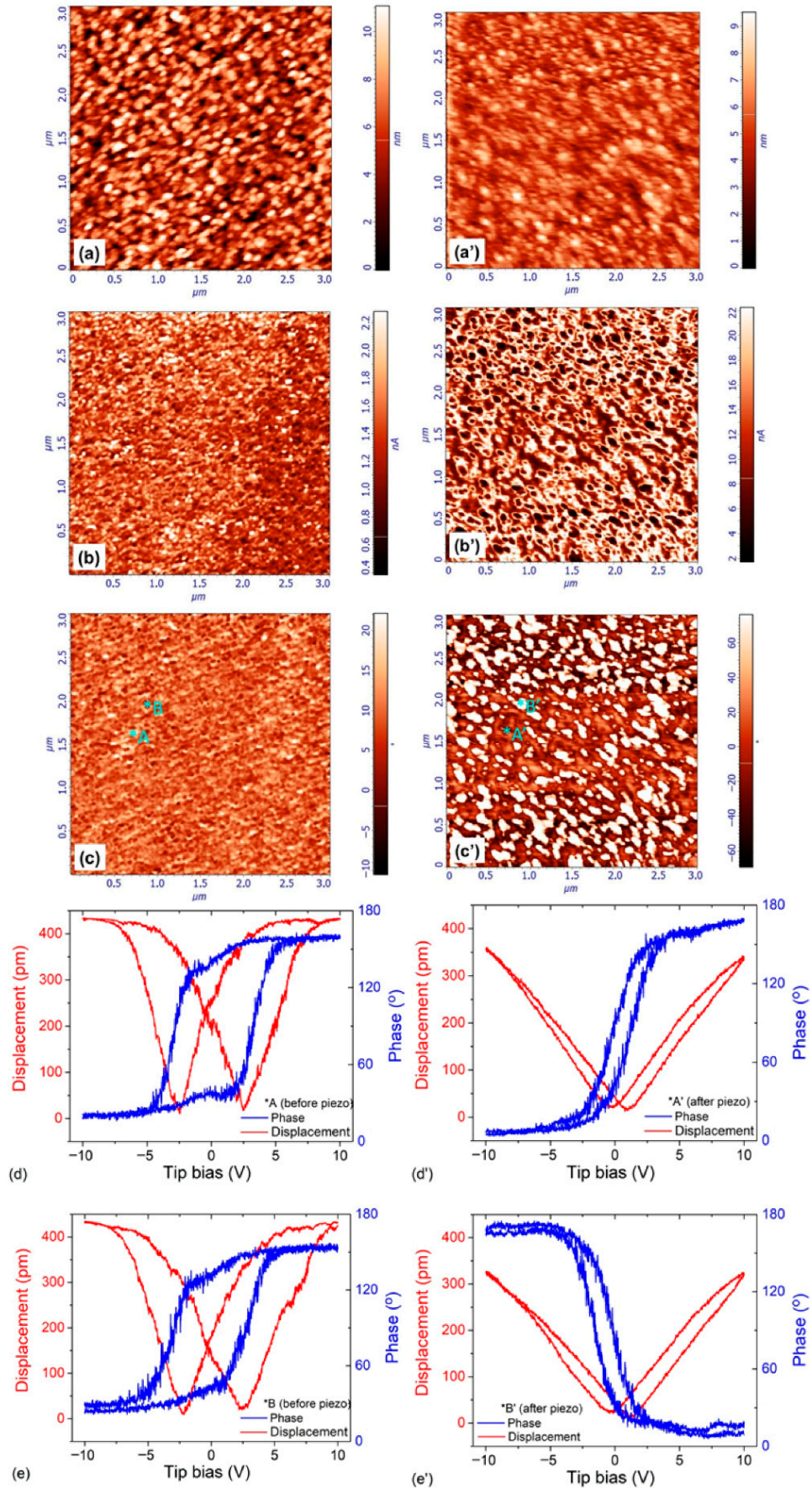


Figure 5. PFM results of the BFCO thin film before (left side—(**a**–**e**)) and after (right side—(**a′**–**e′**)) piezo-photocatalysis experiments.

Local PFM polarization switching spectroscopy tests performed at two distinct points (marked as A′ and B′ in Figure 5c′) highlight different polarizations and orientations of piezoelectric domains. Figure 5d′,e′ show the local PFM amplitude butterfly loop and phase hysteresis curve recorded at these points. Compared to data from the BFCO sample before the degradation test, the piezoresponse signal, the width of the phase hysteresis loops, and the gap between PFM amplitude curves are all about three times smaller. Additionally, the phase hysteresis loops clearly indicate that the polarization and orientation of the piezoelectric domains at points A′ and B′ are opposite.

In this study, the significantly higher piezocatalytic activity compared to photocatalytic activity is linked to the piezo-potential induced by mechanical stress and the reorientation of piezoelectric domains. The piezo-potential can enhance the degradation process by bending energy bands, but the orientation of the piezoelectric domains is also critical. Additionally, the band bending caused by the piezoelectric potential can either counteract or combine with the band bending resulting from ferroelectricity, depending on the direction of the piezoelectric polarization. Based on this understanding, a piezo-photocatalytic mechanism is proposed.

2.2.5. Possible Mechanism for Piezo-Photocatalysis

When the RhB solution with the catalyst was exposed only to visible light, there was a negligible change in RhB concentration (about 2%) over 180 min (Figure 1a). This poor photocatalytic performance indicates that the visible light cannot activate the BFCO catalyst to degrade the organic pollutant. This might be due to an unsuitable band structure, rapid recombination or low mobility of photo-generated charge carriers. XPS measurements show that the valence band energies of the BFCO sample before and after piezocatalysis tests are 1.35 eV and 1.38 eV, respectively (Figure 6).

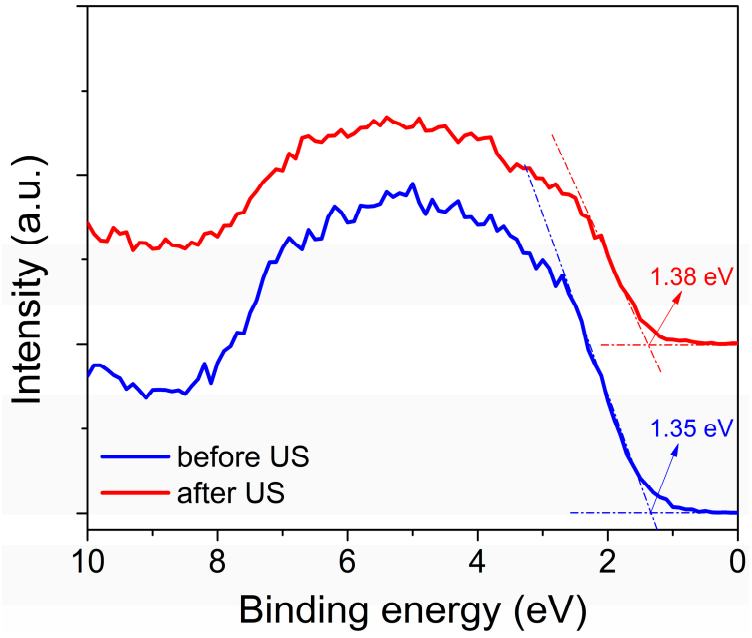


Figure 6. XPS measured valence band spectra of the BFCO sample before and after piezo-photocatalysis.

The band gap energies (E_g) derived from Tauc plots were estimated to be 2.1 eV, both before and after piezo-photocatalysis tests. Accordingly, the conduction bands' positions were determined to be −0.75 eV and −0.72 eV. Scavenger tests on RhB dye degradation indicate that the primary reactive species involved in the process were, in order of importance: $O_2^{\bullet -}$ > $^1O_2$ > $HO^{\bullet}$. In this study, VB position is less positive than HO•/OH^- or H_2O redox potentials (1.99 eV or 2.73 eV vs. NHE), meaning the photo-excited holes

cannot oxidize H_2O or OH^- to generate HO•. On the other hand, the CB edge position, being more negative than the standard reduction potential of $O_2^{\bullet-}/O_2$ (E = −0.33 eV vs. NHE), supports the reduction reaction. However, poor photocatalytic performance could be due to the improper orientation of piezo/ferroelectric dipoles. The lack of phase contrast shown in Figure 5c suggests that piezo/ferroelectric domains have a preferential orientation, likely with negative charges facing the substrate. XRD results (Figure 3) show that the as-deposited BFCO thin film exhibits a preferred crystallographic growth direction along the (111) planes. $BiFeO_3$ is a ferroelectric material with significant spontaneous polarization along the $[111]_c$ direction [43], which is equivalent to $[001]_{hex}$ (Figure 7a). The preferential orientation of the ferroelectric domains could be ascribed to the epitaxial stress developed during film growth.

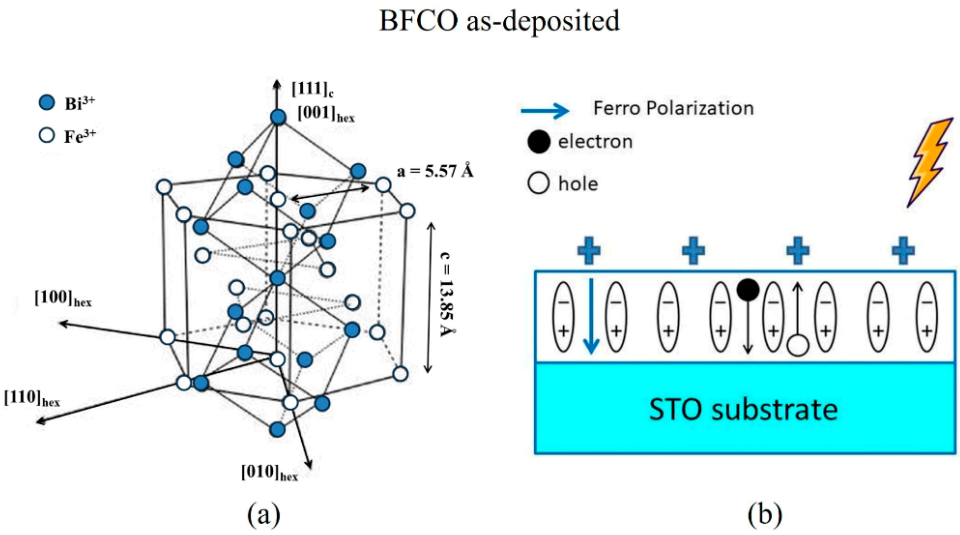


Figure 7. Crystallographic structure of $BiFeO_3$ (**a**) and schematic illustration of the proposed mechanisms in the ferroelectric sample during photocatalysis (**b**).

Internal stress in the sample could lead to increased interfacial polarizability due to a large number of defect states (such as oxygen vacancies) [44]. These defects may trap free charge carriers and form dipoles, resulting in enhanced polarization [45]. The ferroelectric polarization field causes spatial separation of photo-excited charge carriers, with holes accumulating on the catalyst surface and electrons at the substrate–film interface (Figure 7b). Although the CB edge position supports the water oxidation reaction O_2/H_2O (E = 1.23 eV vs. NHE), the inability of photo-excited electrons to engage in the $O_2^{\bullet-}/O_2$ reduction reaction limits photodegradation performance. The $O_2^{\bullet-}$ reactive species can also generate other reactive oxygen species (ROS), such as $^1O_2$ and HO•, which might further enhance photodegradation. Since the VB edge position (E = 1.35 eV) is less positive than the water oxidation reaction HO•/H_2O (E = 1.99 eV), the holes available at the surface of the catalyst cannot participate in the degradation process. Thus, the inadequate VB edge position and orientation of ferroelectric dipoles are the main reasons for poor photocatalytic performance.

Interestingly, this limitation in photodegradation performance was overcome by reversing piezoelectric domains through lattice strain relaxation induced by mechanical vibrations.

PFM measurements conducted after piezo-photocatalysis tests indicate that some of the piezoelectric domains have reversed, and the local piezoresponse is significantly reduced (Figure 5c′–e′). Additionally, XRD measurements performed after piezo-photocatalysis tests show a phase transformation process in the BFCO film, shifting from a monoclinic structure with a preferential (111) orientation to a polycrystalline hexagonal

phase. This change in piezoelectric domains corresponds to an inversion of the crystallographic structure of BFO, as illustrated in Figure 8a,d.

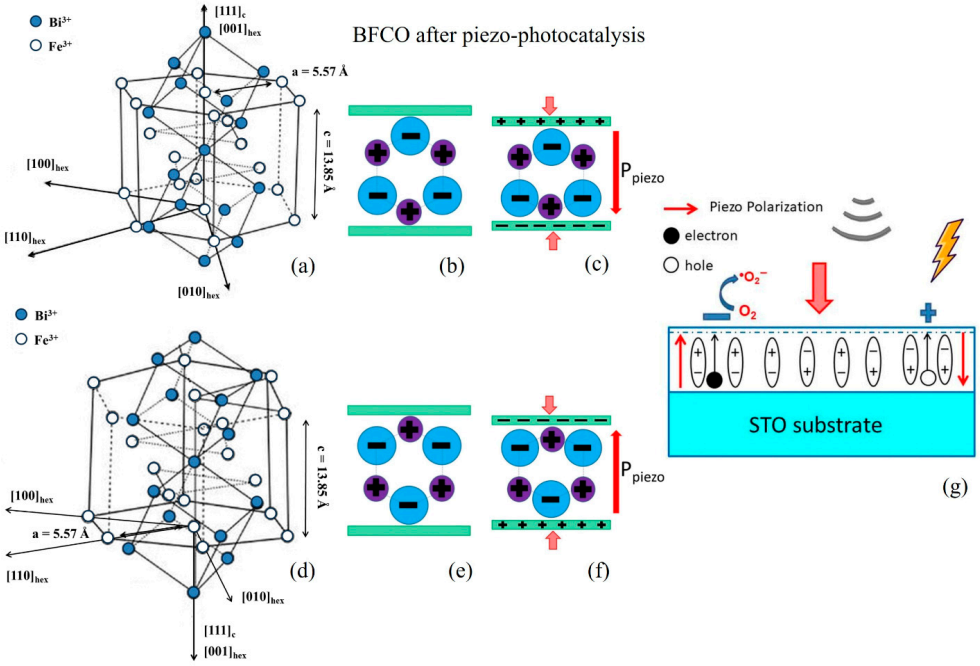


Figure 8. Crystallographic structure of $BiFeO_3$ (**a**,**d**) and schematic illustration of the working principle of piezoelectric (**b**,**c**,**e**,**f**) and ferroelectric photocatalytic device (**g**).

When mechanical strain is applied, a downward piezoelectric polarization and corresponding piezoelectric field are generated in the unreversed piezoelectric domains (as shown in Figure 8c). In contrast, an upward piezoelectric polarization occurs in the reversed piezoelectric domains (Figure 8f). The reversing of these piezoelectric domains might be connected to the lattice strain relaxation process and to the thermally activated migration of oxygen vacancies during piezocatalysis testing. Under US vibrations, the long-range interactions among structural dipoles are strengthened, enhancing oxygen vacancy migration. This, in turn, leads to strain relaxation and the reversing of polarization [46]. The upward piezoelectric polarization causes the positively charged oxygen vacancies to move toward the top surface, compensating for the negative polarization charge. These statements are supported by the XPS results, which indicate that after photo-piezocatalysis tests, the oxygen vacancies peak (O_V) decreased from 36.8% to 24.4%, while surface absorbed oxygen peak (O_A) increased from 13.1% to 21.45%. PFM measurements (Figure 5c′–e′) also confirm the reversing of piezoelectric domains, showing that under an external electric field, the piezoelectric domains at points A′ and B′ exhibit opposite orientations/polarizations. In the case of downward piezoelectric polarization, the piezo-photo-generated electrons and holes are separated and move in opposite directions, leading to the accumulation of electrons at the film–substrate interface. Conversely, with upward piezoelectric polarization, electrons accumulate at the catalyst's free surface and can participate in redox reactions (Figure 8g). Therefore, under mechanical vibration, a lattice strain relaxation process and a change in piezoelectric polarization direction may occur. The upward piezoelectric polarization and the resulting piezoelectric field can drive the spatial separation and transport of electrons towards the catalyst's surface, leading to spatially separated redox reactions and enhanced piezo-photocatalytic efficiency. These statements are further supported by the stability and reusability tests of the catalyst (Figure 1d), which show better piezo-photodegradation performance for the next three consecutive runs.

The piezo-photo-generated electrons, which accumulate on the free surface of the piezo-catalyst, react with O_2 in water to produce $O_2^{\bullet-}$ radicals. These radicals are the primary active species responsible for RhB degradation. The resultant $O_2^{\bullet-}$ could react with water to generate $^1O_2$ and $OH^\bullet$ active species [22], or combine with H^+ to produce $^1O_2$ [11]. All these reactive species ($O_2^{\bullet-}/^1O_2/OH^\bullet$) contribute to RhB degradation:

$$e^- + O_2 \rightarrow O_2^{\bullet-} \quad (1)$$

$$2O_2^{\bullet-} + H_2O \rightarrow H_2O_2 + 2\,HO^- + {}^1O_2 \quad (2)$$

$$O_2^{\bullet-} + H_2O_2 \rightarrow OH^\bullet + OH^- + {}^1O_2 \quad (3)$$

$$2O_2^{\bullet-} + 2H^+ \rightarrow H_2O_2 + {}^1O_2 \quad (4)$$

$$O_2^{\bullet-}/{}^1O_2/OH^\bullet + RhB \rightarrow \text{byproducts} \quad (5)$$

On the other hand, Fe^{2+} sites could donate their electrons to adsorbed molecular oxygen, generating $O_2^{\bullet-}$ radicals, or they can activate H_2O_2 to produce •OH radicals through a heterogeneous Fenton reaction. Fe^{2+} active sites are regenerated by accepting piezo-electrons [19,23]. XPS analysis shows that some Fe^{2+} is oxidized to Fe^{3+} during the photo-piezocatalysis process, its proportion decreasing from 67.9% to 57.0%.

$$Fe^{2+} + O_2 \rightarrow Fe^{3+} + O_2^- \quad (6)$$

$$Fe^{2+} + H_2O_2 \rightarrow Fe^{3+} + OH^- + OH^\bullet \quad (7)$$

$$Fe^{3+} + e^- \rightarrow Fe^{2+} \quad (8)$$

Hydroxyl radicals, $OH^\bullet$, generated in the presence of Fe^{2+} and $O_2^{\bullet-}$ and light are the main cause of Cr^{3+} oxidation. The $OH^\bullet$ radicals react with the chromium complex Cr^{3+} leading to the formation of Cr^{6+} [47]:

$$Cr^{3+} + 3\,OH^\bullet \rightarrow Cr^{6+} + 3OH^- \quad (9)$$

Cr^{6+} can be reduced to Cr^{3+} in the presence of Fe^{3+} by the following reaction:

$$Fe^{3+} + Cr^{6+} = Cr^{3+} + 3Fe^{2} \quad (10)$$

Furthermore, the high piezoelectric potential observed in the BFCO sample could also cause energy band bending. This band bending, induced by the piezoelectric polarization of BFCO, may either counteract or amplify the band bending caused by ferroelectricity, depending on the polarization directions of piezoelectric/ferroelectric domains. At the negatively charged surface of BFCO, the CB bends upward, while in the positively charged region, the VB bends downward. The potential energy and, consequently, the degradation rate are influenced by the piezoelectric field generated through mechanical deformation. A higher piezoelectric potential can cause greater band bending, which could significantly enhance the piezo-degradation rate in the dark. When the catalyst is exposed to both visible light and ultrasonic vibrations, its piezo-photodegradation performance improves only slightly, increasing from 83.7% under just ultrasonic irradiation to 86.2% with the addition of light irradiation. Although the number of thermally or acoustically activated carriers is much smaller than that of light-excited carriers, the fast recombination rate of photo-generated charges means that the catalyst's piezo-photodegradation activity is only slightly better than its piezo-degradation performance. It appears that the presence of piezoelectric domains with opposite orientations promotes the recombination of photo-excited electrons

and holes at the interface, limiting the ability of the piezoelectric process to further enhance the photocatalytic decomposition.

In the literature, various possible photocatalytic degradation pathways of RhB have been proposed through byproducts analysis (LC-MS and GC-MS) and active species trapping experiments (ESR analysis) [48–50]. For example, Yang et al. proposed two possible pathways for the photocatalytic degradation of RhB over a TS-1/C_3N_4 composite under visible light. In the first pathway, RhB is attached by •OH radicals and undergoes N-deethylation to form the intermediate DP1 (m/z = 415), followed by further oxidation leading to intermediated DP2 (m/z = 245) and DP3 (m/z = 167) through the cleavage of the double bond and tertiary amine, while DP2 is further decomposed to DP4 (m/z = 111). In the second pathway, the positive amino group of the RhB molecule is initially attacked by •O_2^- radicals and decomposed to DP5 (m/z = 314), which is subsequently oxidized by •OH to produce DP6 (m/z = 111). Ultimately, the reaction intermediates from both pathways (DP4 and DP6) are further degraded into small molecular compounds [48]. Similarly, two routes have been proposed by Harikumar et al. in the photodegradation of RhB using a visible light active $CoNiO_2$–$BiFeO_3$–NiS ternary nanocomposite [51]. In one pathway, •OH radicals cleave the central C–C bond of RhB, leading to the formation of N, N-diethyl-N′-ethylated intermediate, which is further decomposed into 3-hydroxy naphthalic acid (m/z = 166). Subsequent structural breakdown produces 4-hydroxy benzoic acid (m/z = 135). In an alternative pathway, the RhB molecule is degraded into an intermediate (m/z = 282) by C-N cleavage, which is further transformed into compounds with m/z values of 268 and 254 via carboxylation processes. Ultimately, the intermediates from both pathways are oxidized into low-molecular-weight compounds such as phthalic acid, benzoic acid, 3,4-dihydroxybenzoic acid, and adipic acid. Thus, the catalytic degradation of organic compounds typically proceeds through N-deethylation, hydroxylation, carboxylation, ring opening, and eventual mineralization [52].

3. Materials and Methods

3.1. Synthesis of Thin Film

Chromium-doped bismuth ferrite (BFCO) thin film was deposited onto $SrTiO_3$ (STO) substrate by reactive high-power impulse magnetron sputtering (HiPIMS) technology. A commercially available Bi_2FeCr alloy disk (50.4 mm diameter, 3.18 mm thickness) was used as source material (magnetron's target) and placed in the deposition vacuum chamber. Before the sputtering process, a 10^{-4} Pa base pressure was achieved using preliminary and turbomolecular pumps. Prior to the deposition process, the target was pre-sputtered for 15 min to remove any contaminants present on its surface and to establish stable operational conditions for the reactive deposition process. The pressure of the Ar:O_2 (20:1) gas mixture was maintained at 0.75 Pa, and the target–substrate distance was 8 cm. The negative discharge pulses of 700 V amplitude and 5 μs duration were applied on the cathode with a frequency of 1.5 kHz. The very short pulse duration was set in order to limit ion back-attraction effect [53] and to suppress arcing during the reactive HiPIMS process [54]. To generate the required electrical pulses, a pulsing unit (home-built high-power pulse generator) was utilized, receiving a constant voltage from a DC power supply. It should be noted that during the negative voltage pulse, a peak current of approximately 15 A was achieved. During deposition, the substrate temperature was kept constant at 700 °C, while the deposition time was set to 40 min to achieve a film' s thickness of 200 nm. The film's thickness was measured using a Veeco DEKTAK (Veeco, Dornach Munich, Germany) profilometer.

3.2. Photo-, Piezo- and Photo-Piezocatalytic Degradation Experiments

The synthesized BFCO/STO system was evaluated for the degradation of RhB dye (R6626, Merck(Sigma-Aldrich, Darmstadt, Germany)), a commonly studied organic contaminant, from aqueous solution through photo-, piezo-, and photo-piezocatalysis. The tests were performed in a 3 cm diameter glass Petri dish containing 3 mL of RhB solution (5 mg/L in distilled water), with a molar absorption coefficient of 1.05×10^5 L/mol/cm at 554 nm. For photodegradation experiments, the BFCO/STO catalyst (1×1 cm^2) was immersed in the solution and placed horizontally under a visible lamp ($\lambda > 400$ nm) with an incident light flux of 25 mW/cm^2. For piezocatalytic activity measurements, the same catalysis-glass vessel system was placed in an ultrasonic cleaner operating at 37 kHz with an output power of 80 W. A mixture of water and ice was used as the ultrasonic medium to prevent temperature-induced degradation and to avoid pyrocatalytic effects. When studying piezo-photocatalytic efficiency, both the ultrasonic cleaner and the visible light source were used simultaneously.

Before each experiment, the RhB aqueous solution and catalyst were kept in the dark for 30 min to achieve the adsorption–desorption equilibrium. Following light irradiation and/or exposure to mechanical waves, the residual concentrations of RhB at fixed 30 min intervals were determined using a standard calibration curve (Figure S2). The measurements were carried out using an ONDA V-10 Plus spectrophotometer at the maximum absorption wavelength (λ_{max} = 554 nm), while the UV-Vis spectrum of the RhB solution in the range of 190 nm–650 nm was recorded using a UV-1901 instrument (Beijing Puxi General Instrument Co., Ltd., Beijing, China). The degradation efficiency was calculated using the equation: RhB degradation (%) = $(1 - C_t/C_0) \times 100$, where C_0 is the RhB initial concentration (after 30 min in the dark), and C_t is the residual dye concentration after a certain irradiation time.

The degradation rate value was estimated from the linear fit of the $-\ln(C/C_0)$ vs. time plot. For quenching experiments, commercially available (Sigma Aldrich, Darmstadt, Germany) p-benzoquinone (BQ, 0.5 mM), ethylenediaminetetraacetic acid disodium salt (EDTA-2Na, 2 mM), isopropanol (IPA, 5 mM), and sodium azide (NaN_3, 1 mM) were separately mixed into the RhB aqueous solution before catalytic degradation in order to suppress the contribution of superoxide radicals ($O_2^{\bullet -}$), holes (h^+), hydroxyl radicals ($HO^{\bullet}$) and singlet oxygen ($^1O_2$), respectively.

3.3. Film Characterization

To gain a deeper understanding of the processes occurring during pollutant degradation experiments, the structural, chemical, and piezo-/ferroelectric properties of the BFCO sample were analyzed before and after piezo-photocatalysis tests. Crystallographic ordering and structural features were examined using X-ray diffraction (XRD). Diffraction patterns in the 10–70° 2θ range were recorded using a Shimadzu LabX XRD-6000 Diffractometer (Shimadzu, Kyoto, Japan) (CuK_α radiation), in Bragg–Brentano configuration, with a scan speed of 1°/min. Structural parameters were determined through line profile fitting using HighScore X'Pert software v5.3a. The oxidation states in the BFCO thin film were analyzed using an ESCALB Xi + XPS system (Thermo Fisher Scientific, Waltham, MA, USA), employing a monochromated Al K_α X-ray source (1486.6 eV). The binding energy values have been calibrated using the carbon C-1s peak (284.6 eV) as a reference. High resolution spectra of the Bi-4f, Fe-2p, Cr-2p, and O-1s peaks were fitted using a non-linear least-squares method (Multi Pak 8.2 C software) with a Gaussian–Lorentzian function. A dual beam of low-energy Ar^+ ions and low-energy electrons was employed during data acquisition for charge neutralization. To remove surface contaminants, prior to XPS spectra acquisition a 5 min 500 eV Ar ion sputtering step was conducted. Ruther-

ford backscattering spectrometry (RBS) experiments were performed to determine the BFCO thin film's stoichiometry. A detailed description of the analytical method can be found in a previous paper [55]. FTIR spectra were registered in transmission mode using a FTIR VERTEX 70 spectrometer (Bruker Optics, Ettlingen, Germany). Changes in piezoelectric and ferroelectric properties were assessed using Piezoresponse Force Microscopy (PFM) with an NT-MDT Solver-Pro multi-mode scanning probe microscope (NT-MDT, Moscow, Russia) [56].

4. Conclusions

Photo-, piezo- and piezo-photocatalytic experiments for Rhodamine B degradation were conducted on Cr-doped bismuth ferrite thin films deposited on a $SrTiO_3$ substrate by reactive HiPIMS. The highest contaminant removal was achieved when both visible light and mechanical vibrations were applied simultaneously. After 180 min of exposure, the efficiency increased to 86.2%, with a reaction rate of $11.3 \cdot 10^{-3}$ min^{-1} (16.1 times higher than that observed during photocatalysis). Scavenger tests, where different reagents were added to the contaminated solution, revealed that superoxide radicals ($O_2^{\bullet -}$) played the primary role in the degradation process, followed by $^1O_2$ and $HO^{\bullet}$. Further analysis on the sample properties revealed structural, chemical and ferroelectric changes induced during piezo-photocatalytic experiments. While the main structure in the as-deposited film was the monoclinic phase with a preferential growth direction, the diffractograms recorded after piezo-photocatalysis showed a predominantly polycrystalline film with a hexagonal type structure. Additionally, XPS measurements indicated that the sample's surface underwent oxidative processes. PFM amplitude and phase images recorded before the contaminant degradation tests showed a lack of contrast, indicating a downward polarization orientation of the piezoelectric domains. During piezo-photocatalysis, some of the piezoelectric domains were reversed through a lattice strain relaxation process, and changes in polarization direction were clearly observed in the PFM phase image. The reduced photocatalytic degradation response was attributed to the combined effects of an improper band structure (determined from XPS and UV-VIS spectroscopy measurements) and the downward orientation of the piezoelectric domain polarization, which impeded the generated electrons from reacting with O_2 in the water to produce $O_2^{\bullet -}$ radicals. These radicals were found to be the major contributors to RhB degradation. The proposed mechanism for the piezocatalysis experiments involves local atomic displacement generated by ultrasonic waves, leading to the lattice strain relaxation, reversal of internal polarization field and, consequently, to a significant improvement in RhB degradation efficiency.

Supplementary Materials: The following supporting information can be downloaded at: https://www.mdpi.com/article/10.3390/catal16050379/s1, Figure S1: The Fourier transform infrared spectra of the BFCO/STO sample before and after use as a catalyst for the photo-piezocatalytic degradation of RhB dye for 180 min.; Figure S2: Calibration curve of RhB dye and UV-Vis spectrum of a 5 mg/L aqueous RhB solution.

Author Contributions: Conceptualization, R.J., G.B. and V.T.; methodology, G.B. and V.T.; validation, R.J., G.B. and V.T.; formal analysis, R.J., M.D., T.M., V.C., G.B. and V.T.; investigation, G.B. and V.T.; resources, G.B.; data curation, R.J., V.C., G.B. and V.T.; writing—original draft preparation, R.J., G.B. and V.T.; writing—review and editing, R.J., I.-L.V., G.B. and V.T.; supervision, G.B. and V.T.; project administration, G.B.; funding acquisition, I.-L.V., G.B. and V.T. All authors have read and agreed to the published version of the manuscript.

Funding: This research received no external funding.

Data Availability Statement: Data Availability Statements are available in manuscript.

Acknowledgments: The authors acknowledge the support provided by the project "Integrated interdisciplinary system for the implementation of sustainable development activities in the North-East Region of Romania—SIDNER" (Cod SMIS: 337821), project co-funded through the Regional Program North-East 2021–2027, Investment priority: PRNE_P1, A more competitive, more innovative region, Call: RDI activities in collaboration with SMEs and investments in public RDI organizations and universities, oriented towards the needs identified in the regional entrepreneurial discovery process, Project call number: PR/NE/2024/P1/RSO1.1/1/2–RDI INFRASTRUCTURES. This work was financially supported by the Ministry of Education and Research, CNCS-UEFISCDI, project number PN–III–P1-1.1-TE-2021-0265, within PNCDI III program. Ion beam experiments have been performed at 3 MV Tandetron accelerator from "Horia Hulubei" National Institute for Physics and Nuclear Engineering (IFIN-HH) and were supported by the Romanian Governmental Programme through the National Programme "Instalații și Obiective de Interes Național".

Conflicts of Interest: The authors declare no conflicts of interest.

References

1. Sun, X.; Xian, T.; Li, R.; Yang, H. Heterojunction interface field and piezoelectric polarization field cooperatively facilitating photocarrier separation in heterojunction piezo-photocatalysts: Experimental and theoretical characterization. *Colloids Surf. A Physicochem. Eng. Asp.* **2023**, *677*, 132430. [CrossRef]
2. Li, H.; Li, F.; Shen, Z.; Han, S.T.; Chen, J.; Dong, C.; Chen, C.; Zhou, Y.; Wang, M. Photoferroelectric perovskite solar cells: Principles, advances and insights. *Nano Today* **2021**, *37*, 101062. [CrossRef]
3. Jing, Q.; Liu, Z.; Cheng, X.; Li, C.; Ren, P.; Guo, K.; Yue, H.; Xie, B.; Li, T.; Wang, Z.; et al. Boosting piezo-photocatalytic activity of $BiVO_4$/$BiFeO_3$ heterojunctions through built-in polarization field tailoring carrier transfer performances. *Chem. Eng. J.* **2023**, *464*, 142617. [CrossRef]
4. Meng, W.; Hu, R.; Yang, J.; Du, Y.; Li, J.; Wang, H. Influence of lanthanum-doping on photocatalytic properties of $BiFeO_3$ for phenol degradation. *Chin. J. Catal.* **2016**, *37*, 1283–1292. [CrossRef]
5. Niu, F.; Chen, D.; Qin, L.; Zhang, N.; Wang, J.; Chen, Z.; Huang, Y. Facile Synthesis of Highly Efficient p–n Heterojunction CuO/$BiFeO_3$ Composite Photocatalysts with Enhanced Visible-Light Photocatalytic Activity. *ChemCatChem* **2015**, *7*, 3279–3289. [CrossRef]
6. Domanski, K.; Correa-Baena, J.P.; Mine, N.; Nazeeruddin, M.K.; Abate, A.; Saliba, M.; Tress, W.; Hagfeldt, A.; Gratzel, M. Not All That Glitters Is Gold: Metal-Migration-Induced Degradation in Perovskite Solar Cells. *ACS Nano* **2016**, *10*, 6306–6314. [CrossRef] [PubMed]
7. Steirer, K.X.; Schulz, P.; Teeter, G.; Stevanovic, V.; Yang, M.; Zhu, K.; Berry, J.J. Defect Tolerance in Methylammonium Lead Triiodide Perovskite. *ACS Energy Lett.* **2016**, *1*, 360–366. [CrossRef]
8. Sando, D.; Barthélémy, A.; Bibes, M. $BiFeO_3$ epitaxial thin films and devices: Past, present and future. *J. Phys. Condens. Matter* **2014**, *26*, 473201. [CrossRef] [PubMed]
9. Tiron, V.; Jijie, R.; Matei, T.; Velicu, I.-L.; Gurlui, S.; Bulai, G. Piezo-Enhanced Photocatalytic Performance of Bismuth Ferrite-Based Thin Film for Organic Pollutants Degradation. *Coatings* **2023**, *13*, 1416. [CrossRef]
10. Nechache, R.; Harnagea, C.; Li, S.; Cardenas, L.; Huang, W.; Chakrabartty, J.; Rosei, F. Bandgap tuning of multiferroic oxide solar cells. *Nat. Photonics* **2015**, *9*, 61–67. [CrossRef]
11. Lan, S.; Yu, C.; Sun, F.; Chen, Y.; Chen, D.; Mai, W.; Zhu, M. Tuning piezoelectric driven photocatalysis by La-doped magnetic $BiFeO_3$-based multiferroics for water purification. *Nano Energy* **2022**, *93*, 106792. [CrossRef]
12. Boughelout, A.; Khiat, A.; Macaluso, R. Photocatalysis of Methyl Orange (MO), Orange G (OG), Rhodamine B (RhB), Violet and Methylene Blue (MB) Under Natural Sunlight by Ba-Doped $BiFeO_3$ Thin Films. *Materials* **2025**, *18*, 887. [CrossRef]
13. Zargazi, M.; Entezari, M.H. BFO thin film on the stainless steel mesh by anodic EPD: A visible light photocatalyst for degradation of Rhodamin B. *J. Photochem. Photobiol. A Chem.* **2018**, *365*, 185–198. [CrossRef]
14. Ramezanalizadeh, H.; Manteghi, F. Design and development of a novel $BiFeO_3$/$CuWO_4$ heterojunction with enhanced photocatalytic performance for the degradation of organic dyes. *J. Photochem. Photobiol. A Chem.* **2017**, *338*, 60–71. [CrossRef]
15. Fourmont, P.; Cloutier, S.G. Screen-printed p–n BiOCl/$BiFeO_3$ heterojunctions for efficient photocatalytic degradation of Rhodamine B. *RSC Adv.* **2022**, *12*, 24868–24875. [CrossRef]
16. Yuan, B.; Wu, J.; Qin, N.; Lin, E.; Bao, D. Enhanced Piezocatalytic Performance of (Ba,Sr)TiO_3 Nanowires to Degrade Organic Pollutants. *ACS Appl. Nano Mater.* **2018**, *1*, 5119–5127. [CrossRef]
17. Nhan Nguyen, T.N.; Chang, K.S. Piezoelectricity-enhanced multifunctional applications of hydrothermally-grown p-$BiFeO_3$–n-ZnO heterojunction films. *Renew. Energy* **2022**, *197*, 89–100. [CrossRef]

18. Roy, J.; Roy, S.; Mondal, D.; Bag, N.; Chowdhury, J.R.; Ghosh, S.; Bardhan, S.; Mondal, R.; Basu, R.; Das, S. Gd-doped bismuth ferrite nanocomposite: A promising candidate for piezocatalytic degradation of organic dyes and pathogenic *E. coli*. *Surf. Interfaces* **2024**, *44*, 103579. [CrossRef]
19. Su, C.; Li, R.; Li, C.; Wang, W. Piezo-promoted regeneration of Fe^{2+} boosts peroxydisulfate activation by $Bi_2Fe_4O_9$ nanosheets. *Appl. Catal. B* **2022**, *310*, 121330. [CrossRef]
20. Zhang, R.; Wu, X.; Li, Y.; Shao, W.; Zhang, Y.; Liu, Z.; Nie, J.; Tan, J.; Ye, W. Enhanced piezo-photocatalytic performance by piezoelectric and visible light photoexcitation coupling through piezoelectric $Na_{0.5}Bi_{0.5}TiO_3$ micron crystals. *RSC Adv.* **2020**, *10*, 7443–7451. [CrossRef] [PubMed]
21. Marin, R.; Oussta, F.; Katea, S.N.; Prabhudev, S.; Botton, G.A.; Westin, G.; Hemmer, E. Europium-doped ZnO nanosponges—Controlling optical properties and photocatalytic activity. *J. Mater. Chem. C* **2019**, *7*, 3909–3919. [CrossRef]
22. Acharya, S.; Mansingh, S.; Parida, K.M. The enhanced photocatalytic activity of g-C_3N_4-$LaFeO_3$ for the water reduction reaction through a mediator free Z-scheme mechanism. *Inorg. Chem. Front.* **2017**, *4*, 1022–1032. [CrossRef]
23. Su, C.; Li, C.; Li, R.; Wang, W. Insights into highly efficient piezocatalytic molecule oxygen activation over $Bi_2Fe_4O_9$: Active sites and mechanism. *Chem. Eng. J.* **2022**, *452*, 139300. [CrossRef]
24. Huang, Y.; Zhang, X.; Zhu, G.; Gao, Y.; Cheng, Q.; Cheng, X. Synthesis of silver phosphate/sillenite bismuth ferrite/graphene oxide nanocomposite and its enhanced visible light photocatalytic mechanism. *Sep. Purif. Technol.* **2019**, *215*, 490–499. [CrossRef]
25. Chen, X.; Li, A.; Xing, L.; Wang, J.; Sun, Y.; Wang, Y.; Chen, G.; Xing, T.; Xu, L. Piezo-photocatalytic degradation and mechanism of rhodamine B by flexible $MoSe_2$/PVDF composite foam. *J. Water Process Eng.* **2024**, *59*, 105015. [CrossRef]
26. Hu, J.; Chen, Y.; Zhou, Y.; Zeng, L.; Huang, Y.; Lan, S.; Zhu, M. Piezo-enhanced charge carrier separation over plasmonic Au-BiOBr for piezo-photocatalytic carbamazepine removal. *Appl. Catal. B Environ.* **2022**, *311*, 121369. [CrossRef]
27. Chen, G.; Chen, J.; Pei, W.; Lu, Y.; Zhang, Q.; Zhang, Q.; He, Y. Bismuth ferrite materials for solar cells: Current status and prospects. *Mater. Res. Bull.* **2019**, *110*, 39–49. [CrossRef]
28. Jang, H.M.; Han, H.; Lee, J.H. Spin-coupling-induced improper polarizations and latent magnetization in multiferroic $BiFeO_3$. *Sci. Rep.* **2018**, *8*, 405. [CrossRef] [PubMed]
29. Heon Kim, Y.; Bhatnagar, A.; Pippel, E.; Alexe, M.; Hesse, D. Microstructure of highly strained $BiFeO_3$ thin films: Transmission electron microscopy and electron-energy loss spectroscopy studies. *J. Appl. Phys.* **2014**, *115*, 105015. [CrossRef]
30. Diéguez, O.; González-Vázquez, O.E.; Wojdeł, J.C.; Íñiguez, J. First-principles predictions of low-energy phases of multiferroic $BiFeO_3$. *Phys. Rev. B Condens. Matter. Mater. Phys.* **2011**, *83*, 094105. [CrossRef]
31. Hatt, A.J.; Spaldin, N.A.; Ederer, C. Strain-induced isosymmetric phase transition in $BiFeO_3$. *Phys. Rev. B Condens. Matter. Mater. Phys.* **2010**, *81*, 054109. [CrossRef]
32. Chen, Z.; Qi, Y.; You, L.; Yang, P.; Huang, C.W.; Wang, J.; Sritharan, T.; Chen, L. Large tensile-strain-induced monoclinic M_B phase in $BiFeO_3$ epitaxial thin films on a $PrScO_3$ substrate. *Phys. Rev. B* **2013**, *88*, 054114. [CrossRef]
33. Selbach, S.M.; Einarsrud, M.A.; Grande, T. On the Thermodynamic Stability of $BiFeO_3$. *Chem. Mater.* **2009**, *21*, 169–173. [CrossRef]
34. Zeches, R.J.; Rossell, M.D.; Zhang, J.X.; Hatt, A.J.; He, Q.; Yang, C.H.; Ramesh, R. A strain-driven morphotropic phase boundary in $BiFeO_3$. *Science* **2009**, *326*, 977–980. [CrossRef]
35. Zhang, M.H.; Shen, C.; Zhao, C.; Dai, M.; Yao, F.Z.; Wu, B.; Hinterstein, M. Deciphering the phase transition-induced ultrahigh piezoresponse in (K, Na) NbO_3-based piezoceramics. *Nat. Commun.* **2022**, *13*, 3434. [CrossRef] [PubMed]
36. Dixit, H.; Beekman, C.; Schlepütz, C.M.; Siemons, W.; Yang, Y.; Senabulya, N.; Clarke, R.; Chi, M.; Christen, H.M.; Cooper, V.R. Understanding Strain-Induced Phase Transformations in $BiFeO_3$ Thin Films. *Adv. Sci.* **2015**, *2*, 1500041. [CrossRef] [PubMed]
37. Sun, F.; Chen, D.; Gao, X.; Liu, J.M. Emergent strain engineering of multiferroic $BiFeO_3$ thin films. *J. Materiomics* **2021**, *7*, 281–294. [CrossRef]
38. Sharma, V.; Ghosh, R.K.; Kuanr, B.K. Investigation of room temperature ferromagnetism in transition metal doped $BiFeO_3$. *J. Phy. Condens. Mat.* **2019**, *31*, 395802. [CrossRef]
39. Ait Ali, B.; Bouhmouche, A.; Wendling, L.; Hu, C.; Bouillet, C.; Schmerber, G.; Saeedi, A.M.; Zafeiratos, S.; Papaefthimiou, V.; Moubah, R.; et al. Impact of film thickness on the structural, linear and non-linear optical properties of ferroelectric Bi_2FeCrO_6 perovskite thin films. *Vacuum* **2023**, *216*, 112411. [CrossRef]
40. Yamashita, T.; Hayes, P. Analysis of XPS spectra of Fe^{2+} and Fe^{3+} ions in oxide materials. *Appl. Surf. Sci.* **2008**, *254*, 2441–2449. [CrossRef]
41. Wu, H.; Pei, Z.; Xia, W.; Lu, Y.; Leng, K.; Zhu, X. Structural, magnetic, dielectric and optical properties of double-perovskite Bi_2FeCrO_6 ceramics synthesized under high pressure. *J. Alloys Compd.* **2020**, *819*, 153007. [CrossRef]
42. Zhao, X.; Yang, Q.; Cui, J. XPS study of surface absorbed oxygen of ABO_3 mixed oxides. *J. Rare Earths* **2008**, *26*, 511–514. [CrossRef]
43. You, H.; Wu, Z.; Zhang, L.; Ying, Y.; Liu, Y.; Fei, L.; Chen, X.; Jia, Y.; Wang, Y.; Wang, F.; et al. Harvesting the Vibration Energy of $BiFeO_3$ Nanosheets for Hydrogen Evolution. *Angew. Chem. Int. Ed.* **2019**, *58*, 11779–11784. [CrossRef]
44. Roy, S.; Bardhan, S.; Pal, K.; Ghosh, S.; Mandal, P.; Das, S.; Das, S. Crystallinity mediated variation in optical and electrical properties of hydrothermally synthesized boehmite (γ-AlOOH) nanoparticles. *J. Alloys Compd.* **2018**, *763*, 749–758. [CrossRef]

45. Roy, S.; Maity, A.; Mandal, P.; Chanda, D.K.; Pal, K.; Bardhan, S.; Das, S. Effects of various morphologies on the optical and electrical properties of boehmite nanostructures. *CrystEngComm* **2018**, *20*, 6338–6350. [CrossRef]
46. Zhou, Y.; Xiong, K.; Wu, S.; Tu, L.; Wang, X.; Chen, Y.; Wu, S.; Zeng, J.; Zheng, Y.; Gu, S.; et al. Anomalous polarization-switching phenomena and noteworthy pyroelectricity in ferroelectric $Hf_{0.5}Zr_{0.5}O_2$ polycrystalline films. *Mater. Today Phys.* **2024**, *43*, 101414. [CrossRef]
47. Yen, C.-C.; Chen, K.-Y.; Ahmed, M.M.M.; Syu, C.-H.; Liu, Y.-T.; Hsieh, Y.-C.; Jien, S.-H.; Tzou, Y.M. Photochemical oxidation of Cr(III) to Cr(VI) in the presence of Fe(III): Influence of Fe(III) concentration and UV wavelength. *J. Hazard. Mater.* **2025**, *485*, 136852. [CrossRef] [PubMed]
48. Yang, J.; Zhu, H.; Peng, Y.; Li, P.; Chen, S.; Yang, B.; Zhang, J. Photocatalytic Performance and Degradation Pathway of Rhodamine B with TS-1/C3N4 Composite under Visible Light. *Nanomaterials* **2020**, *10*, 756. [CrossRef] [PubMed]
49. Fu, J.; Liang, F.; Zhong, W.; Kuang, T.; Yin, Z.; Li, Y.; Huang, Z.; Liu, H.; Ma, D. Enhanced catalytic degradation activity through quenching introduces Pd doping in TiO_2 derived from NH2-MIL-125(Ti). *Environ. Res.* **2025**, *285*, 122387. [CrossRef]
50. Ma, D.; Liang, F.; Xue, Q.; Liu, Y.; Zhuang, C.; Li, S. Interfacial engineering of $Cd_{0.5}Zn_{0.5}S$/BiOBr S-scheme heterojunction with oxygen vacancies for effective photocatalytic antibiotic removal. *Acta Phys.-Chim. Sin.* **2025**, *41*, 100190. [CrossRef]
51. Harikumar, B.; Okla, M.K.; Alaraidh, I.A.; Mohebaldin, A.; Soufan, W.; Abdel-Maksoud, M.A.; Aufy, M.; Thomas, A.M.; Raju, L.L.; Khan, S.S. Robust visible light active $CoNiO_2$–$BiFeO_3$–NiS ternary nanocomposite for photo-fenton degradation of rhodamine B and methyl orange: Kinetics, degradation pathway and toxicity assessment. *J. Environ. Manag.* **2022**, *317*, 115321. [CrossRef]
52. Ma, D.; Xue, Q.; Liu, Y.; Liang, F.; Li, W.; Liu, T.; Zhuang, C.; Zhao, Z.; Li, S. Manipulating interfacial charge redistribution in Mn0.5Cd0.5S/N-rich C3N5 S-scheme heterojunction for high-performance photocatalytic removal of emerging contaminants. *J. Mater. Sci. Technol.* **2026**, *243*, 265–274. [CrossRef]
53. Velicu, I.-L.; Tiron, V.; Popa, G. Dynamics of the fast-HiPIMS discharge during FINEMET-type film deposition. *Surf. Coat. Technol.* **2014**, *250*, 57–64. [CrossRef]
54. Tiron, V.; Velicu, I.-L.; Matei, T.; Cristea, D.; Cunha, L.; Stoian, G. Ultra-Short Pulse HiPIMS: A Strategy to Suppress Arcing during Reactive Deposition of SiO_2 Thin Films with Enhanced Mechanical and Optical Properties. *Coatings* **2020**, *10*, 633. [CrossRef]
55. Tiron, V.; Jijie, R.; Dumitru, I.; Cimpoesu, N.; Burducea, I.; Iancu, D.; Borhan, A.; Gurlui, S.; Bulai, G. Piezo-ferroelectric response of bismuth ferrite based thin films and their related photo/piezocatalytic performance. *Ceram. Int.* **2023**, *49*, 20304–20314. [CrossRef]
56. Tiron, V.; Jijie, R.; Matei, T.; Cimpoesu, N.; Bulai, G. Tuning chemical composition and structural properties of bismuth ferrite based thin films by reactive bipolar HiPIMS. *Ceram. Int.* **2024**, *50*, 46663–46672. [CrossRef]

Disclaimer/Publisher's Note: The statements, opinions and data contained in all publications are solely those of the individual author(s) and contributor(s) and not of MDPI and/or the editor(s). MDPI and/or the editor(s) disclaim responsibility for any injury to people or property resulting from any ideas, methods, instructions or products referred to in the content.